Monthly Notices
of the
ROYAL ASTRONOMICAL SOCIETY

Mon. Not. R. Astron. Soc. **427,** 956–967 (2012) doi:10.1111/j.1365-2966.2012.21947.x

The physical parameters of the microquasar S26 in the Sculptor Group galaxy NGC 7793

M. A. Dopita,[1,2]★ J. L. Payne,[3] M. D. Filipović[3] and T. G. Pannuti[4]

[1]*Research School of Astronomy and Astrophysics, Australian National University, Cotter Road, Weston, ACT 2611, Australia*
[2]*Department of Astronomy, King Abdulaziz University, PO Box 80203, Jeddah, Saudi Arabia*
[3]*University of Western Sydney, School of Computing, Engineering and Mathematics, Locked Bag 1797, Penrith South DC, NSW 2751, Australia*
[4]*Department of Earth and Space Sciences, Space Science Center, Morehead State University, Morehead, KY 40351, USA*

Accepted 2012 August 15. Received 2012 August 9; in original form 2012 April 19

ABSTRACT

NGC 7793−S26 is an extended source (350 pc × 185 pc) previously studied in the radio, optical and X-ray domains. It has been identified as a microquasar which has inflated a superbubble. We used integral-field spectra from the Wide-Field Spectrograph on the ANU 2.3-m telescope to analyse spectra between 3600 and 7000 Å. This allowed us to derive fluxes and line ratios for selected nebular lines. Applying radiative shock model diagnostics, we estimate shock velocities, densities, radiative ages and pressures across the object. We show that S26 is just entering its radiative phase, and that the northern and western regions are dominated by partially radiative shocks due to a lower density interstellar medium in these directions. We determine a velocity of expansion along the jet of 330 km s^{-1}, and a velocity of expansion of the bubble in the minor axis direction of 132 km s^{-1}. We determine the age of the structure to be 4.1 × 10^5 yr, and the jet energy flux to be (4–10) × 10^{40} erg s^{-1}. The jet appears to be collimated within ∼0.25°, and to undergo very little precession. If the relativistic $\beta \sim 1/3$, then some 4 $M_\odot$ of relativistic matter has already been processed through the jet. We conclude that the central object in S26 is probably a black hole with a mass typical of the ultraluminous X-ray source population which is currently consuming a fairly massive companion through Roche lobe accretion.

Key words: stars: winds, outflows – ISM: abundances – ISM: bubbles – ISM: jets and outflows – galaxies: individual: NGC 7793 – X-rays: binaries.

1 INTRODUCTION

The Sculptor Group galaxy NGC 7793 is a SA(s)d spiral galaxy located at RA (J2000) 23^{h}57^{m}49^s.83, Dec. −32^{d}35^{m}27^s.7. It has a distance estimated from the tip of its red giant branch (RGB) of 3.6 Mpc (Jacobs et al. 2009) or 3.44 Mpc estimated from its Cepheid stars (Pietrzynski et al. 2010). The foreground Galactic extinction $E(B-V)$ is estimated at 0.019 mag (Schlegel, Finkbeiner & Davis 1998). In this paper, we adopt a distance of 3.5 Mpc.

The elongated H II region within it, N7793−S26, was discovered by Blair & Long (1997) using interference filters isolating the Hα + [N II] lines and the [S II] lines in order to identify supernova remnants (SNRs). They described the object as a extended oval emission region with a high [S II] to Hα ratio and a size of 185 × 350 pc (based on the distance of 3.5 Mpc rather than the 3.38 Mpc used in their paper). The major axis of this nebula is oriented south-east to north-west direction. They noted there was no evidence of an interior star cluster, but they suggested that multiple supernovae (SNe) may be in the process of creating a superbubble, which would account for its unusually large size.

Read & Pietsch (1999) reported X-ray observations of P8 coincident within 3 arcsec to N7793−S26, best fitted by a low-temperature thermal model. They could not rule out the possibility of time variability as seen in their fig. 4 *ROSAT* light curves. Very Large Array (VLA) radio observations at 6 and 20 cm followed, and were reported in Pannuti et al. (2002). They noted that the object is composed of both a bright point and extended source, designated together as S26. Their discussion of the object is quite extensive, noting it to be the only evolved stellar candidate in N7793 detected in the X-ray, optical and radio domains. The object was seen in *Chandra* and spatially resolved as a triple source for the first time by Pakull, & Grisé (2008), and was further studied by Pakull, Soria & Motch (2010) and Soria et al. (2010). Later, Pannuti et al. (2011) also detected the X-ray counterpart to S26 in their analysis of the *Chandra* data obtained in NGC 7793.

Pakull, & Grisé (2008) noted that a significant fraction of ultra-luminous X-ray (ULX) sources appear to be embedded in extended

★E-mail: michael.dopita@anu.edu.au

(∼100 pc) bubbles of shocked gas, and they identified N7793−S26 as belonging to this class of objects. Pakull et al. (2010) further suggested that N7793−S26 is powered by black hole with a pair of jets, similar to SS433; but twice as large and more powerful. They suggest that S26 has a structure similar to a Fanaroff–Riley type II active galaxy with a X-ray and optical core, X-ray hotspots and radio lobes encased in an optical and X-ray cocoon. The core can be fitted by a power law in the 0.3–10 keV energy band, and has a luminosity of $L_{0.3-10} \approx 7 \times 10^{36}$ erg s^{-1}. There are two X-ray bright hotspots on either side of the central source, which appear to be thermal in nature with a combined luminosity of $L_{0.3-10} \approx 1.8 \times 10^{37}$ erg s^{-1}. Using He II narrow-band observations, they find significant emission at 4686 Å ($He^{2+} \rightarrow He^{1+}$) spatially distributed in a similar manner to Hα. A narrow slit spectrum taken near the core suggested an expanding shell with a maximum expansion velocity of ∼250 km s^{-1}.

Soria et al. (2010) used the Australia Telescope Compact Array (ATCA) to resolve the radio lobe structure and to map the spectral index in the radio cocoon of S26. The radio structure is strongly aligned to the axis defined by the three X-ray hotspots While the radio spectral index in the NW and SE lobes is approximately −0.7 to −0.6, it is flatter (−0.4 to 0.0) across most of the cocoon and becomes inverted at the base of the jets near the core (0.0 to +0.4)[1] suggesting a self-absorbed spectrum due to either free–free or Compton self-absorption. The total thermal energy in the bubble is estimated to be ∼10^{53} erg.

In this paper, we present the results of integral-field spectroscopy (IFS) in the wavelength region 3600–7200 Å using the Wide-Field Spectrograph (WiFeS) (Dopita et al. 2007, 2010) mounted on the 2.3-m telescope located at the Siding Spring Observatory. This allows the shock velocity, pre-shock density, ram pressure and radiative age to be derived across the face of the nebula, in turn permitting a much more accurate determination of the fundamental properties of the microquasar which is driving these shocks.

2 OBSERVATIONS AND ANALYSIS

IFS on N7793−S26 was performed on 2009 December 13 at Siding Springs Observatory using the 2.3-m Advanced Technology Telescope and its WiFeS. WiFeS provides a 25 × 38 arcsec^2 field with 0.5 arcsec spatial sampling along each of 25 × 1 arcsec^2 slits. The output format matches the 4096 × 4096 pixel CCD detectors in both the red-side and blue-side cameras, and the instrument sensitivity is optimized for the blue and red sides of the spectrum reaching a throughput (top of atmosphere to back of camera) of 35 per cent. We used the RT560 beam splitter. The blue spectral range covers 3200–5900 Å, at a spectral resolution of $R \sim 3000$ (≈100 km s^{-1}). In the red, the range is 5300–9800 Å, and the resolution is $R \sim 7000$ (≈45 km s^{-1}).

Three 1000-s exposures of S26 were taken under photometric conditions at PA (measured east of north) 145°. The estimated seeing was excellent, ≈1.3 arcsec. Standard and telluric stars, flat-field, bias and wavelength calibration data frames were also obtained on the same evening.

The data were reduced using the WiFeS data reduction pipeline based on National Optical Astronomy Observatory (NOAO) IRAF software. This data reduction package was developed from the Gemini IRAF package (McGregor et al. 2003). Use of the pipeline consists of four primary tasks: WIFES to set environment parameters; WFTABLE to convert single-extension FITS file formats to multi-extension FITS ones and create file lists used by subsequent steps; WFCAL to process calibration frames including bias, flat-field, arc and ÒwireÓ; and WFREDUCE to apply calibration files and create data cubes for analysis. We used the standard star HD 26169 for flux calibration and the bright B-type star HIP 8352 for any necessary telluric corrections.

In Fig. 1 we show a false colour RGB image of N7793−S26 in its proper orientation to the sky. There is intense [S II] emission in the south-western hotspot, associated with the termination shock of the jet from the central object as seen in X-rays (Pakull et al. 2010). The elliptical shell of the bubble is, by contrast, much brighter in [O III] and the [O III]/Hβ ratio increases as the Balmer line flux decreases. The shell brightness decreases going north on the eastern side, and is incomplete on its western side. This together with the asymmetry in the distance of the NW X-ray hotspot compared to the SW hotspot from the central X-ray source strongly suggest a systematic gradient in the density of the interstellar medium (ISM), highest towards the SW side, and lower towards the NE. This is reminiscent of the gradient seen across the system SS433–W50 in the Galaxy (Zealey, Dopita & Malin 1980).

The other emission regions appearing in this figure [the green region close to 23:58:00.5 −32:33:18 (J2000)] and the turquoise regions in the general vicinity of 23:57:59.7 −32:40:00 (J2000) are H II regions which are unassociated with S26. These are useful in constraining the chemical abundances in the shock modelling described in the next section.

The spectrum of the most intense 2 × 2 arcsec^2 region is shown in Fig. 2. A classic shock-excited spectrum is revealed with both strong [O I] and [S II] emission relative to Hα and velocity-broadened line profiles in all of the emission lines. This spectrum can be compared with that of the emission region in SS443 (Zealey et al. 1980, fig. 2), in which the velocity dispersion is much lower, but the forbidden lines are much stronger with respect to Hα. The difference can be ascribed to two factors: first a much lower characteristic shock velocity in SS433 and second, lower chemical abundances in the ISM in S26.

Using QFitsView[2] we were able to create a Voronoi tessellation diagram based on a 30:1 Hα signal-to-noise ratio (S/N) ratio using the red data cube as shown in Fig. 3. This was later used as a template to extract one-dimensional spectra from NGC 7793−S26. After extraction, the IRAF task SPLOT allowed the determination of emission line flux and the velocity width based on Gaussian fits to the Hα line profile. Photometric measurement errors were calculated based on the rms noise estimated for each spectra; varying between an average of 2 per cent for the stronger λ6563 line and 23 per cent for the weaker λ6364 line.

In Table 1, we present flux densities (in units of 10^{-15} erg cm^{-2} s^{-1}) for selected emission lines corresponding to the Voronoi extraction by number listed in Fig. 3. The lines are labelled at rest wavelength and include Hβ (λ4861), [O III] (λλ4959, 5007), [O I] (λλ6300, 6364), [N II] (λλ6550, 6585), Hα (λ6563) and [S II] (λλ3716, 3731). Also included are log ratios [O III]λ5007/Hβ, [N II]λ6585/Hα, [S II]λλ6716, 6731/Hα and Hα surface brightness (erg s^{-1} cm^{-2} sr^{-1}).

[1] Spectral index here is defined as α, for $S_\nu \propto \nu^\alpha$, where S_ν is flux density and ν is frequency.

[2] Written by Thomas Ott and freely available at www.mpe.mpg.de/∼ott/dpuser/index.html.

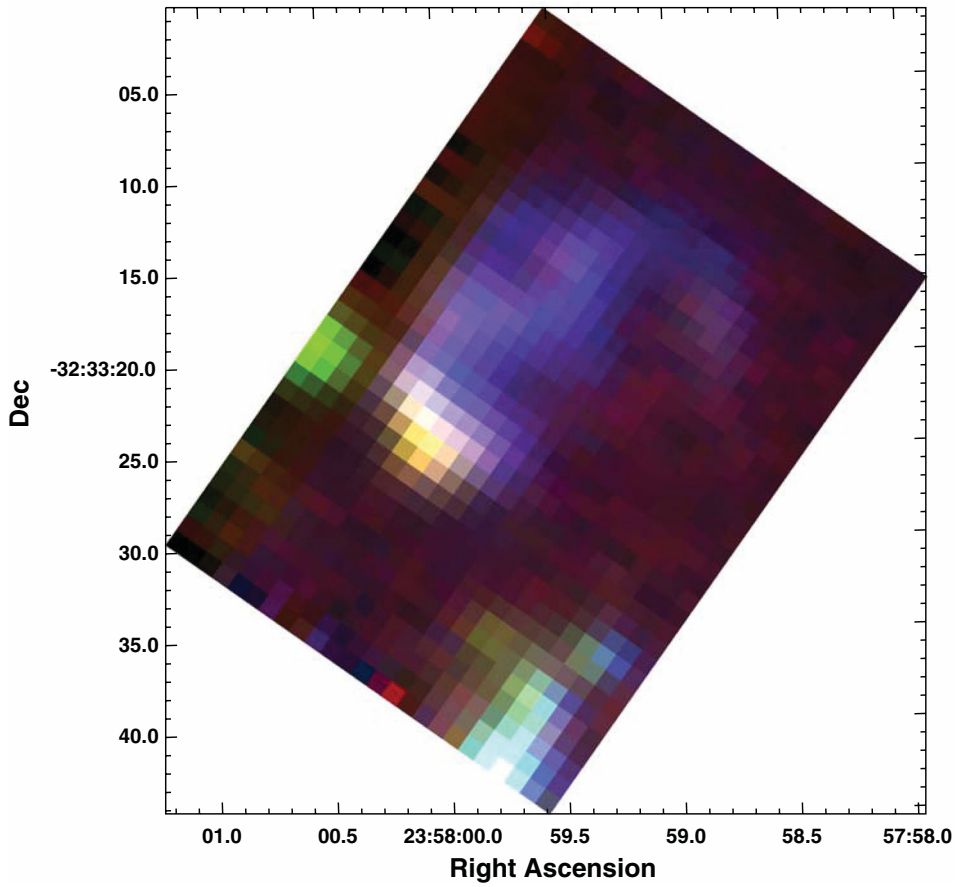

Figure 1. RGB ([S II], Hα, [O III] λ5007) false colour image of NGC 7793−S26. The *y*-axis has been rebinned to a final resolution of 1 × 1 arcsec, and the coordinates given are for epoch J2000. The purpose of this image is to map these three emission regions for visual inspection. However, the strength of the [S II] and Hα lines in the SE jet region is apparent, as is the relative strength of the [O III] lines in the fainter parts of the shell. The regions used for analysis are shown in Fig. 3, and quantitative values for each of these emission lines in these regions can be found in Table 1.

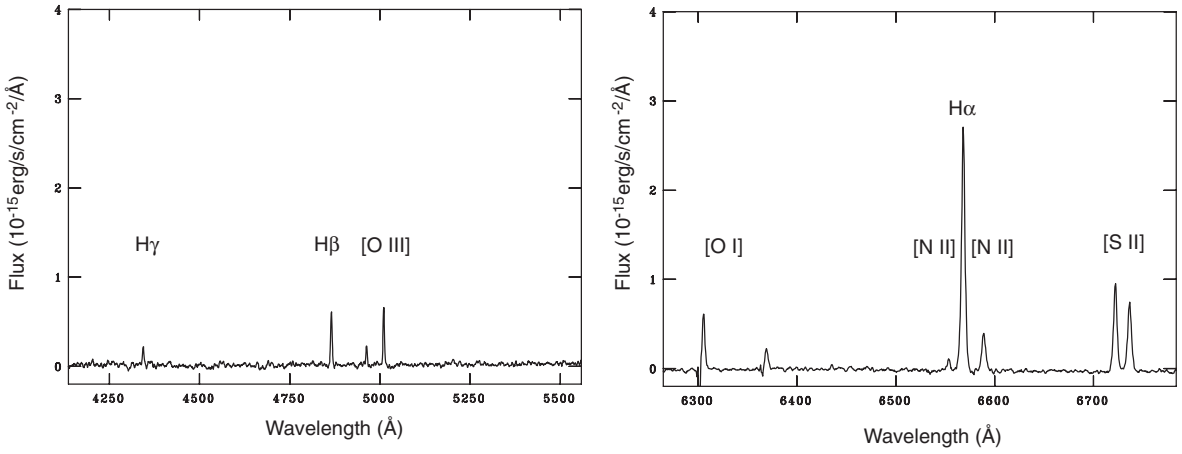

Figure 2. One-dimensional spectra of brightest 2 × 2 arcsec^2 region in N7793−S26. Note the large velocity dispersion in the lines. Note also that the N7793−S26 emission lines are redshifted (∼228 km s^{-1}) consistent with the reported redshift of N7793 (227 km s^{-1}; Koribalski et al. 2004).

3 SHOCK ANALYSIS OF S26

Although the SE region of S26 shows a very normal shock-excited spectrum, the relatively strong [O III] emission in the northern part of the shell is harder to explain. There are two possible explanations – either that this region is ionized by X-rays emanating from the central source, or that these regions contain only partially radiative shocks which enhance the relative strength of the [O III] lines by cutting off the emission that would arise from the recombination zone of the shock. Such shocks were first considered by Dopita & Binette (1983) in the context of the SNRs IC 443 and RCW 86, and the general behaviours of the line ratios of these 'truncated' shocks were given. Later, Raymond et al. (1988) made a more complete study, and investigated the effects of density and shock velocity.

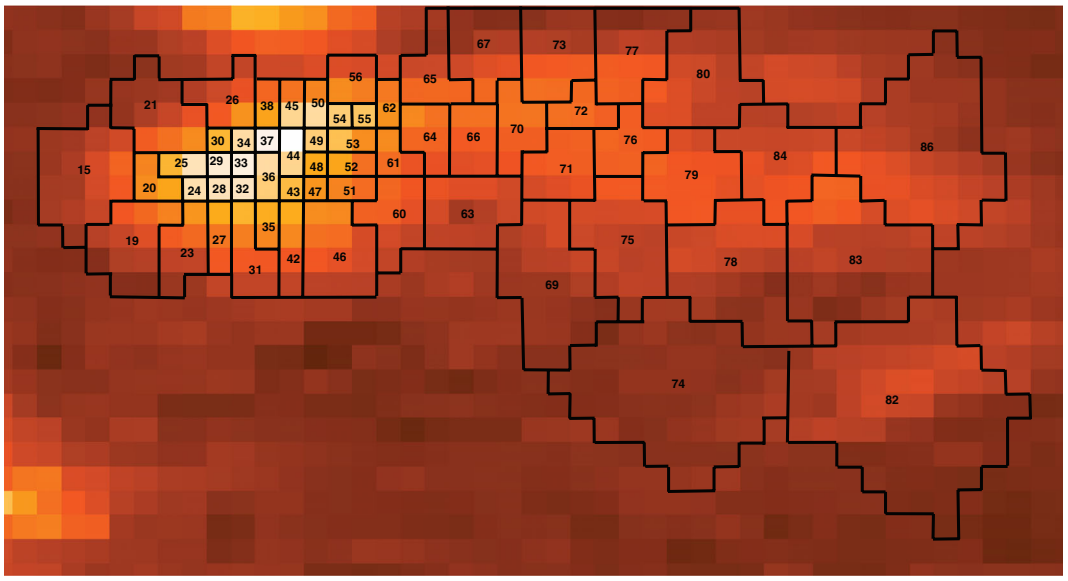

Figure 3. A portion of the elected Voronoi regions used for sampling overlaid on to part of the WiFeS Hα image. The 0.5 × 1.0 arcsec pixel of the WiFeS instrument have 'stretched' this image in the horizontal direction compared with Fig. 1. The regions 5, 6, 10, 12 and 13 are a complex of H II regions, unassociated with S26. Apart from region 13 these are mostly located off the edge of this image in the lower left region. These H II regions were used to calibrate the chemical abundances appropriate to the analysis of S26.

The possibility that the nebula is predominantly X-ray ionized can be readily eliminated on energetic grounds. The integrated luminosity of the X-ray sources in S26 is no greater than about 3×10^{37} erg s^{-1} from observations taken with the *Chandra* satellite (Pakull et al. 2010). From the same reference, the Hβ luminosity of S26 is given as $\sim 1 \times 10^{38}$ erg s^{-1}. For comparison, the sum of the Hβ flux in all the regions shown in Fig. 3 is 5.5×10^{37} erg s^{-1}. However, we are probably missing some of the flux, so we adopt the Pakull et al. (2010) value here. Models for photoionized nebulae with an abundance of $Z = 0.5\,Z_{\odot}$, appropriate to this region of NCG 7793, emit about 50 times the flux observed at Hβ (López-Sánchez et al. 2012). Therefore, the total nebular luminosity has to be of the order of 5×10^{39} erg s^{-1} – over 100 times the observed X-ray luminosity.

Apart from these energetic constraints, if X-rays were dominating the excitation, the strength of the [O I] lines should be much greater in the SE portion of the nebula, since X-ray-excited nebulae are characterized by extended warm, partially ionized tails in their H II regions. This is expected on the basis of theoretical models as described in Dopita & Sutherland (2003), and a fine example of this phenomenon was observed by Pakull & Mirioni (2002) in the source Ho II X-1.

We can therefore conclude that the spectral characteristic of the northern part of the nebula may be better explained by partially radiative shocks. This would be consistent with the evidence described above arguing for a lower pre-shock density in this part of the nebula. We now proceed to investigate this idea in more detail.

3.1 The shock models

The H II regions identified in Fig. 3 enable us to determine the appropriate chemical abundance set. We have used the shock/photoionization code MAPPINGS IIIS, an updated version of the code originally described in Sutherland & Dopita (1993) to generate the models described in López-Sánchez et al. (2012). We then used the line strengths reported in Table 1 and the modified strong-line technique also described in López-Sánchez et al. (2012) to constrain the abundance in this region of NGC 7793; $Z = 0.5 \pm 0.2\,Z_{\odot}$. We therefore adopt $Z = 0.5\,Z_{\odot}$ for our subsequent analysis of S26.

With this abundance set, we have run a grid of partially radiative shock models. The shock velocity was varied from 100 to 220 km^{-1}, and the shock age was constrained by the condition that log ([O III] λ5007/Hβ) < 1.0. We have assumed that the magnetic field pressure and the gas pressure are in equilibrium in the pre-shock gas, with an assumed pre-shock temperature of 10 000 K. For a pre-shock hydrogen density of 1.0, this corresponds to a transverse component of the magnetic field of $B = 1.68\,\mu$G.

For all models, we have assumed full pre-ionization of the gas entering the radiative shock. This assumption will be only valid for shock velocities in excess of 100 km s^{-1}, so this is why we have restricted the minimum shock velocity to 100 km s^{-1}.

The key parameters and line fluxes of the models are given in Table 2. Column (1) gives, for each value of the shock velocity, the corresponding shock age, expressed in terms of log (nt), where n is the pre-shock hydrogen density and t is the shock age. All shock models with a given log (nt) will have very similar emission spectra, modulo collisional de-excitation effects in the density-sensitive lines such as [S II]]6717, 31 Å.

Column (2) of Table 2 gives the mean ion-weighted electron density enhancement factor in the zone-emitting [S II]. This ratio of post-shock to pre-shock electron density increases to a maximum as the gas is compressed by radiative cooling in the post-shock region, before decreasing again as the shocked gas recombines, and the electron density decreases. Note that the computed compression factor is larger for younger shocks. This apparently anomalous result is because the [S II] emission comes mostly from the peak of the electron density in the partially radiative shocks, while in the fully radiative shocks the mean [S II] region electron density is much lower due to the recombination zone in the magnetically supported tail of the shock. The maximum gas density compression factor is higher, and can be approximated by $\rho_1/\rho_0 = 2^{1/2}\mathcal{M}_{\rm A}$, where $\mathcal{M}_{\rm A}$ is the Alvén Mach number of the shock.

Table 1. Selected line fluxes (at rest wavelengths) and log ratios for N7793−S26 and the nearby H II region to its south as shown in Fig. 3. Note in the case of [S II]/ Hα, a ratio greater than 0.4 (the classical definition for a region dominated by shock emission; Lasker 1977; Mathewson et al. 1983, 1984, 1985) corresponds to a log value greater than −0.4.

	Emission line flux ($\times 10^{-15}$ erg cm^{-2} s^{-1})										Log				
Spectrum number	4861 Å Hβ	4959 Å [O III]	5007 Å [O III]	6300 Å [O I]	6364 Å [O I]	6550 Å [N II]	6563 Å Hα	6585 Å [N II]	6716 Å [S II]	6731 Å [S II]	5007 Å/4861 Å [O III]/Hβ	6300 Å/6563 Å [O I]/Hα	6585 Å/6563 Å [N II]/Hα	(6716 Å+ 6731 Å)/6563 Å [S II]/Hα	Hα surface brightness (erg s^{-1} cm^{-2} sr^{-1})
5	2.3	0.8	2.8	0.3		1.8	7.5	0.9	1.0	0.7	0.08	−1.34	−0.91	−0.63	−4.31
6	2.4	1.0	2.9	0.3		2.2	6.9	1.2	1.1	0.9	0.08	−1.43	−0.77	−0.55	−4.46
10	1.9	1.0	2.4	0.3		2.6	7.1	1.1	1.0	0.7	0.11	−1.45	−0.80	−0.60	−4.50
12	1.7	0.8	1.8	0.4		2.9	6.5	0.9	1.0	0.8	0.03	−1.17	−0.84	−0.55	−4.64
13	1.7	1.0	2.8	0.2		4.3	7.1	0.8	1.2	0.8	0.21	−1.45	−0.95	−0.54	−4.74
15	1.1	0.6	1.3	0.2		1.9	3.2		0.9	0.7	0.08	−1.15		−0.30	−4.79
19	1.0	0.6	0.9	0.2		1.3	2.2	0.2	0.5	0.4	−0.05	−1.00	−0.97	−0.38	−4.78
20	0.9	0.3	0.8	0.3		0.4	2.6	0.4	0.9	0.9	−0.06	−1.00	−0.81	−0.18	−4.13
21	1.0	0.4	1.0	0.2	0.2	1.2	2.9	0.2	0.7	0.8	0.03	−1.08	−1.17	−0.28	−4.66
23	0.6	0.4	0.8	0.2		0.7	1.7	0.3	0.5	0.3	0.12	−0.86	−0.75	−0.32	−4.61
24	0.3	0.1	0.3	0.2	0.1	0.2	1.4	0.2	0.5	0.4	−0.04	−0.81	−0.85	−0.16	−3.92
25	0.9	0.3	0.7	0.4	0.2	0.3	2.7	0.4	1.0	0.9	−0.08	−0.84	−0.84	−0.16	−3.94
26	0.8	0.5	1.1	0.3	0.2	0.7	1.7	0.3	0.5	0.4	0.15	−0.80	−0.78	−0.30	−4.63
27	0.5	0.3	0.7	0.2	0.1	0.4	1.6	0.4	0.5	0.4	0.15	−0.87	−0.65	−0.23	−4.35
28	0.4	0.1	0.4	0.2	0.1	0.2	1.5	0.2	0.6	0.5	0.03	−0.97	−0.84	−0.15	−3.90
29	0.4	0.2	0.5	0.2	0.1	0.1	1.5	0.2	0.6	0.5	0.03	−0.80	−0.80	−0.15	−3.88
30	0.2	0.1	0.3	0.2	0.0	0.1	0.9	0.1	0.3	0.3	0.02	−0.67	−0.93	−0.16	−4.12
31	0.6	0.4	1.0	0.3	0.2	0.7	2.4	0.4	0.9	0.6	0.22	−0.93	−0.78	−0.21	−4.47
32	0.4	0.1	0.5	0.2	0.1	0.2	1.6	0.2	0.6	0.5	0.03	−1.03	−0.90	−0.19	−3.86
33	0.5	0.2	0.5	0.3	0.1	0.1	1.6	0.3	0.6	0.5	0.05	−0.78	−0.77	−0.15	−3.88
34	0.3	0.2	0.4	0.2	0.1	0.2	1.1	0.2	0.4	0.3	0.12	−0.63	−0.84	−0.16	−4.05
35	0.4	0.3	0.6	0.3	0.1	0.2	1.6	0.3	0.6	0.4	0.17	−0.81	−0.74	−0.20	−4.16
36	0.7	0.4	1.1	0.3	0.2	0.3	2.9	0.5	1.1	0.8	0.19	−0.95	−0.77	−0.18	−3.91
37	0.4	0.2	0.5	0.2	0.1	0.2	1.3	0.2	0.5	0.4	0.14	−0.76	−0.81	−0.19	−3.95
38	0.5	0.4	0.9	0.2	0.1	0.3	1.1	0.2	0.3	0.2	0.27	−0.85	−0.81	−0.32	−4.33
42	0.5	0.3	1.0	0.3	0.2	0.5	2.1	0.3	0.7	0.5	0.25	−0.90	−0.83	−0.26	−4.36
43	0.4	0.2	0.6	0.1	0.1	0.2	1.3	0.3	0.5	0.4	0.18	−0.94	−0.71	−0.18	−3.95
44	0.8	0.5	1.3	0.4	0.2	0.3	3.0	0.5	1.1	0.8	0.20	−0.90	−0.77	−0.19	−3.90
45	0.5	0.4	1.0	0.2	0.1	0.3	1.5	0.3	0.5	0.4	0.28	−0.94	−0.66	−0.25	−4.20
46	1.1	0.8	2.4	0.3	0.4	1.5	4.4	0.8	1.5	1.2	0.36	−1.18	−0.73	−0.21	−4.47
47	0.3	0.2	0.5	0.1	0.1	0.1	1.0	0.2	0.4	0.3	0.25	−1.06	−0.67	−0.16	−4.07
48	0.3	0.2	0.6	0.1		0.1	1.1	0.2	0.4	0.3	0.30	−1.10	−0.84	−0.19	−4.02
49	0.4	0.3	0.7	0.1	0.1	0.2	1.3	0.2	0.5	0.3	0.26	−0.97	−0.73	−0.20	−3.96
50	0.6	0.5	1.4	0.2	0.1	0.3	1.6	0.3	0.5	0.4	0.35	−0.93	−0.72	−0.24	−4.17
51	0.5	0.4	0.9	0.1	0.1	0.2	1.5	0.3	0.7	0.5	0.26	−1.06	−0.66	−0.11	−4.19
52	0.6	0.3	1.1	0.1		0.3	1.6	0.2	0.6	0.5	0.27	−1.14	−0.86	−0.14	−4.15
53	0.7	0.5	1.3	0.3	0.1	0.3	2.0	0.4	0.7	0.5	0.25	−0.91	−0.74	−0.21	−4.06
54	0.4	0.3	0.8	0.1	0.1	0.2	1.1	0.2	0.4	0.3	0.36	−0.88	−0.83	−0.25	−4.01
55	0.3	0.2	0.8	0.1	0.0	0.2	1.1	0.2	0.4	0.3	0.36	−0.91	−0.81	−0.23	−4.04
56	0.8	0.6	1.5	0.1	0.1	0.5	1.6	0.3	0.5	0.4	0.28	−1.06	−0.74	−0.24	−4.46

Table 1 – *continued*

	Emission line flux ($\times 10^{-15}$ erg cm^{-2} s^{-1})											Log			
Spectrum number	4861 Å Hβ	4959 Å [O III]	5007 Å [O III]	6300 Å [O I]	6364 Å [O I]	6550 Å [N II]	6563 Å Hα	6585 Å [N II]	6716 Å [S II]	6731 Å [S II]	5007 Å/4861 Å [O III]/Hβ	6300 Å/6563 Å [O I]/Hα	6585 Å/6563 Å [N II]/Hα	(6716 Å+ 6731 Å)/6563 Å [S II]/Hα	Hα surface brightness (erg s^{-1} cm^{-2} sr^{-1})
60	1.4	0.8	2.2	0.2		0.9	3.5	0.6	1.6	1.2	0.20	−1.20	−0.80	−0.09	−4.43
61	0.6	0.6	1.3	0.1		0.4	1.8	0.3	0.6	0.5	0.37	−1.08	−0.74	−0.20	−4.30
62	0.4	0.4	1.2	0.1		0.3	1.3	0.2	0.5	0.3	0.46	−1.09	−0.78	−0.20	−4.24
63	1.4	1.2	2.6	0.1		1.2	2.9	0.4	1.3	0.9	0.27	−1.33	−0.89	−0.13	−4.64
64	0.9	0.9	2.4	0.1		0.6	2.7	0.3	0.9	0.7	0.44	−1.40	−0.92	−0.25	−4.33
65	0.6	0.7	1.9	0.1		0.8	2.1	0.4	0.6	0.4	0.47	−1.25	−0.72	−0.34	−4.59
66	0.7	1.0	2.6	0.2		0.8	2.5	0.4	0.8	0.6	0.55	−1.07	−0.81	−0.24	−4.44
67	0.8	0.6	1.4	0.2		1.1	2.1	0.5	0.6	0.5	0.25	−1.09	−0.65	−0.32	−4.75
69	1.3	1.1	2.6	0.4		2.4	3.2	0.4	0.9	0.9	0.29	−0.95	−0.88	−0.26	−4.90
70	0.9	1.0	2.9	0.3		0.8	2.9	0.4	0.7	0.6	0.51	−1.03	−0.87	−0.36	−4.39
71	1.0	1.1	3.1	0.2		0.9	2.5	0.4	0.9	0.7	0.51	−1.05	−0.80	−0.18	−4.57
72	0.6	0.7	1.9	0.1	0.1	0.5	1.9	0.4	0.6	0.5	0.51	−1.23	−0.71	−0.25	−4.39
73	0.7	0.8	2.1	0.3		1.4	2.8	0.7	0.8	0.7	0.48	−1.01	−0.62	−0.29	−4.66
74	0.5	1.0	2.3	0.8		5.7	4.0	0.7	1.1	0.7	0.68	−0.72	−0.76	−0.34	−5.16
75	0.9	1.7	3.5	0.1		2.0	3.5	1.0	0.8	0.6	0.59	−1.39	−0.56	−0.38	−4.76
76	0.9	0.8	2.3	0.2	0.1	0.7	2.6	0.4	0.9	0.6	0.41	−1.18	−0.76	−0.24	−4.44
77	0.7	0.7	1.9	0.2		1.5	2.6	0.5	0.8	0.6	0.43	−1.08	−0.72	−0.30	−4.73
78	0.7	1.2	3.1	0.3		2.7	2.9	0.3	0.5	0.5	0.66	−0.95	−0.95	−0.46	−4.98
79	1.6	1.6	4.3	0.3		1.4	4.4	0.7	1.3	1.1	0.44	−1.10	−0.79	−0.26	−4.51
80	1.2	1.4	3.3	0.3		1.9	3.7	0.4	1.0	0.7	0.43	−1.04	−0.94	−0.34	−4.74
82	2.3	1.4	4.1	1.0		7.0	5.7	0.9	1.2	0.8	0.25	−0.76	−0.79	−0.45	−5.08
83	1.8	1.7	4.4	0.8		3.6	4.2	0.6	0.8	0.6	0.39	−0.75	−0.84	−0.48	−4.92
84	1.6	1.3	4.3	0.3		1.7	4.6	0.7	1.1	0.9	0.44	−1.13	−0.80	−0.35	−4.58
86	2.6	2.2	6.4	0.4		4.1	5.3	1.1	1.2	0.8	0.39	−1.12	−0.67	−0.41	−4.91

Table 2. The finite age (partially radiative) shock models. All have a metallicity $0.5\,Z_{\odot}$. Line fluxes are given with respect to Hβ = 1.0.

(1) log (nt) (cm^3 s)	(2) [S II] Comp. factor	(3) log F (Hβ) (erg cm^2 s^{-1} sr^{-1})	(4) He II 4686	(5) [O III] 5007	(6) [O I] 6300	(7) Hα 6563	(8) [N II] 6584	(9) [S II] 6717+31
$V_s = 100\,km\,s^{-1}$								
12.6021	12.0	−5.2206	0.0481	1.2090	0.3544	3.0970	0.3728	2.3861
12.3010	12.8	−5.2251	0.0486	1.2210	0.3581	3.0860	0.3767	2.4111
12.0000	14.7	−5.2410	0.0504	1.2670	0.3707	3.0770	0.3908	2.4910
11.7782	16.9	−5.2640	0.0531	1.3360	0.3767	3.0760	0.4119	2.5240
11.6021	19.3	−5.2991	0.0574	1.4480	0.3606	3.0820	0.4452	2.4720
11.3010	23.8	−5.4150	0.0746	1.8910	0.2869	3.1210	0.5510	2.2865
11.0000	28.2	−5.6755	0.1335	3.4450	0.2082	3.2780	0.7975	2.2044
$V_s = 120\,km\,s^{-1}$								
12.6021	15.8	−5.0593	0.0937	1.4750	0.3956	3.0670	0.4123	2.5420
12.3010	17.0	−5.0625	0.0944	1.4810	0.3983	3.0590	0.4148	2.5590
12.0000	18.8	−5.0748	0.0971	1.5240	0.4092	3.0500	0.4268	2.6250
11.7782	21.9	−5.0938	0.1013	1.5920	0.4133	3.0480	0.4457	2.6430
11.6021	24.3	−5.1219	0.1079	1.6980	0.3934	3.0520	0.4741	2.5690
11.3010	30.6	−5.2461	0.1428	2.2610	0.2915	3.0870	0.5829	2.2906
11.0000	35.5	−5.4814	0.2430	3.8860	0.2101	3.2050	0.7704	2.1584
$V_s = 140\,km\,s^{-1}$								
12.6021	22.8	−4.8116	0.0656	1.3780	0.3733	3.0160	0.4738	2.5500
12.3010	23.6	−4.8132	0.0659	1.3830	0.3747	3.0110	0.4755	2.5600
12.0000	26.2	−4.8215	0.0671	1.4100	0.3815	3.0030	0.4847	2.6050
11.7782	29.8	−4.8375	0.0695	1.4630	0.3810	3.0010	0.5026	2.6060
11.6021	34.1	−4.8710	0.0749	1.5800	0.3463	3.0040	0.5391	2.4950
11.3010	41.5	−5.0405	0.1099	2.3340	0.2346	3.0390	0.6505	2.2247
11.0000	46.8	−5.5030	0.3107	6.7670	0.1524	3.2840	0.9212	2.0544
$V_s = 170\,km\,s^{-1}$								
12.6021	30.3	−4.6190	0.0553	1.0550	0.3997	2.9950	0.5285	2.7290
12.3010	31.4	−4.6193	0.0554	1.0590	0.4010	2.9900	0.5302	2.7380
12.0000	35.1	−4.6286	0.0564	1.0770	0.4066	2.9850	0.5394	2.7720
11.7782	40.0	−4.6414	0.0581	1.1140	0.3935	2.9830	0.5575	2.7180
11.6021	46.7	−4.6853	0.0637	1.2330	0.3312	2.9870	0.6044	2.5350
11.3010	56.8	−5.0327	0.1380	2.7410	0.1890	3.0660	0.7340	2.1844
$V_s = 200\,km\,s^{-1}$								
12.6021	34.5	−4.4695	0.0589	0.8596	0.5061	2.9940	0.6038	2.8170
12.3010	37.2	−4.4731	0.0594	0.8650	0.5102	2.9880	0.6088	2.8410
12.0000	45.7	−4.4870	0.0608	0.8948	0.4868	2.9860	0.6281	2.7320
11.7782	62.1	−4.5893	0.0728	1.1320	0.3173	2.9970	0.7081	2.2227
$V_s = 220\,km\,s^{-1}$								
12.6021	37.8	−4.3539	0.0570	0.7310	0.5367	2.9870	0.6477	2.6650
12.4771	38.9	−4.3551	0.0571	0.7332	0.5381	2.9840	0.6494	2.6730
12.3010	42.6	−4.3558	0.0579	0.7395	0.5417	2.9820	0.6550	2.6860
12.1761	47.0	−4.3640	0.0592	0.7384	0.5293	2.9810	0.5293	2.6210
12.0000	59.1	−4.3875	0.0717	0.7900	0.4315	2.9820	0.6929	2.2801
11.9031	72.9	−4.5020	0.1228	1.0280	0.2858	2.9910	0.7448	1.8693

Column (3) gives the surface brightness of the shock in Hβ for a pre-shock hydrogen density of $1.0\,cm^{-3}$. This will scale in proportion to the pre-shock density.

The remaining columns of Table 2 give the strengths of some important emission lines with respect to Hβ. These clearly show that the effect of decreasing shock age is to strengthen [O III] and to weaken [O I] and [S II], while the strength of [N II] is only slightly affected.

3.2 Comparison with observations

In Fig. 4 we show the computed line ratios compared with the observed line ratios across the face of S26. The observations imply shock velocities in the computed range of the models, 100–220 $km\,s^{-1}$. The finite age models correctly predict the observed correlation between the (stronger) [O III]/Hβ ratios and the (weaker) [O I]/Hα and [S II]/Hα ratios. As expected there is little correlation between the [O III]/Hβ and [N II]/Hα ratios. Qualitatively at least, the interpretation of the data as indicating the presence of partially radiative shocks is confirmed.

The analysis can be made more quantitative by comparing the surface brightness in Hα with the observed [O III]/Hβ ratio. Models predict that for a given shock velocity as the shock becomes less radiative, the [O III]/Hβ ratio should increase while the Hα surface brightness decreases. On the other hand, an increasing shock velocity leads to a higher Hα surface brightness as the

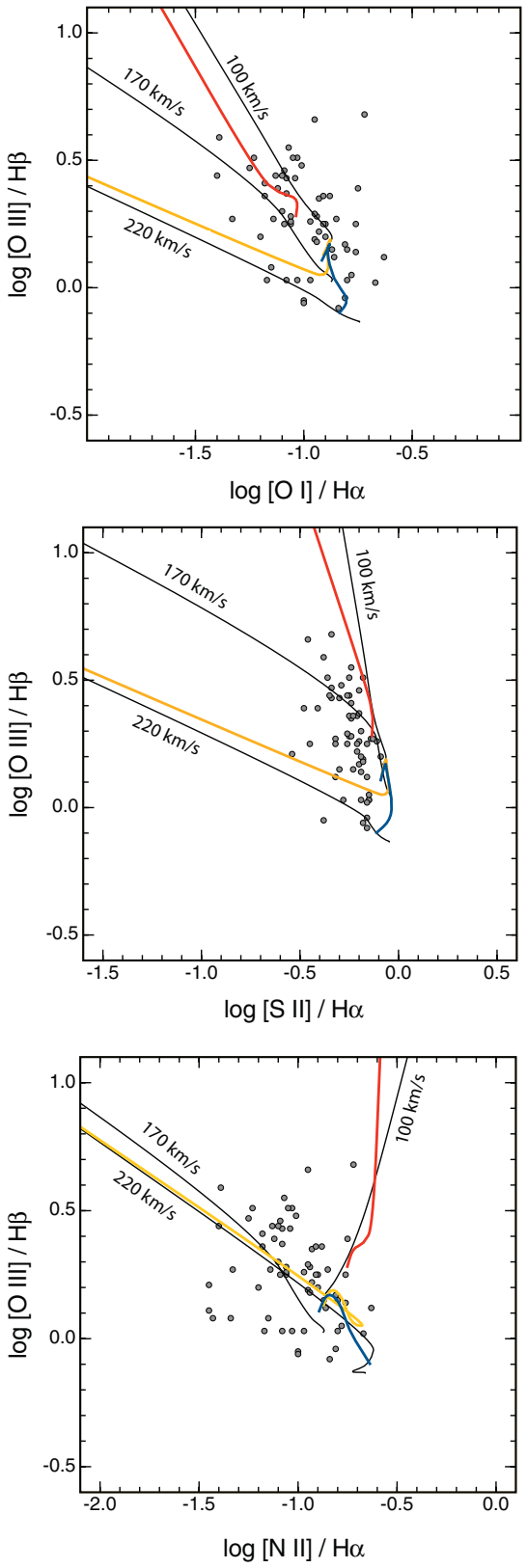

Figure 4. A comparison of the line ratios derived from the partially radiative shock models described in the text with the observational line ratios in S26. For clarity, a number of models have been omitted. The red line is an isochrone for $\log(nt) = 11.3$, the yellow line is for $\log(nt) = 11.6$ and the blue line is for $\log(nt) = 12.6$. These diagnostics are insensitive to age when $\log(nt) > 12.6$.

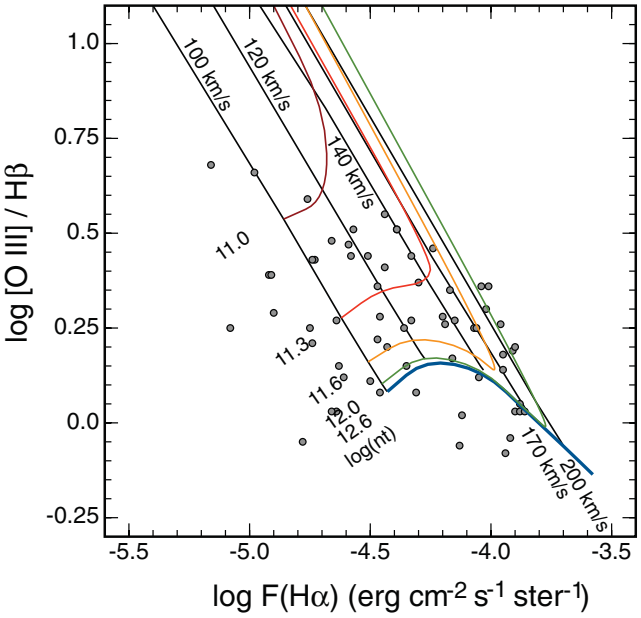

Figure 5. The predicted relationship between the surface brightness in Hα and the [O III]/Hβ ratio as a function of shock velocity and radiative age $\log(nt)$, compared with the observations. Taken at face value, this figure implies shock velocities in the range of 80–220 km^{-1} and radiative ages $\log(nt) > 11$ in S26.

mechanical luminosity of the shock increases, but the models show little variation in the [O III]/Hβ ratio with velocity.

In principle, these facts can be used to independently estimate both the shock velocity, V_s, and the radiative age $\log(nt)$. However, we must first remember that in S26, we are looking through both the front and back of the shell, so we see two shocks along the line of sight. With this correction to the predicted flux we obtain the diagnostics shown in Fig. 5. Here, the measured full width at half-maximum (FWHM) of the observed Hα line has been corrected for the instrumental resolution (50 km s^{-1}) by subtracting it in quadrature. Fig. 5 implies that the lowest shock velocities are of the order of 80 km s^{-1}, while the fastest shocks have $V_s \sim 220$ km s^{-1}.

The shock velocities derived by this technique can be compared with the measured FWHM of the Hα line at the corresponding spatial position. We should not expect a one-on-one correlation between these two values, since the FWHM does not necessarily reflect the actual shock velocity. It will be maximized when we observe two shocks moving in opposite directions, and minimized when we observe a shock travelling transversely to the line of sight. Nonetheless, since the radiative shocks in general are observed moving into denser clouds, and given the fractal distribution of these we might expect some correlation between FWHM and inferred shock velocity. Indeed such a correlation is found, as shown in Fig. 6. We can conclude that the partially radiative shock model provides a good description for the velocity width observations of S26.

3.3 Constraints from He II

Pakull et al. (2010) and Soria et al. (2010) claim (based on narrow-band observations) that there is a strong, extended He II 4686 nebula, of similar size as the Balmer and [[O III]] nebula, and their estimated He II 4686/Hβ flux ratio is ∼0.1. We do not have data of similar sensitivity in the blue part of the spectrum, but an integration across

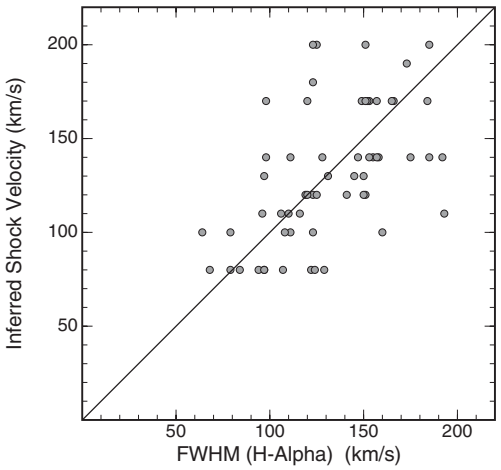

Figure 6. The correlation between the measured FWHM of the Hα line and the shock velocity inferred from Fig. 5. The straight line would represent a one-to-one correlation. The existence of a correlation in this figure helps confirm that the estimated shock velocities are more or less correct.

the nebula gives a flux ratio of He II 4686/Hβ flux $= 0.11 \pm 0.033$, in good agreement with the imaging data quoted above.

Such a value is consistent with the fast shock velocity, $V_s \sim 250\,\mathrm{km\,s^{-1}}$, inferred by Pakull et al. (2010); cf. Dopita & Sutherland (1996, fig. 6). The question we need to resolve here is whether such He II 4686/Hβ flux ratios are also consistent with the partially radiative but slower shocks we infer.

Certainly, strong He II is produced in the precursor zones of fast shocks (Dopita & Sutherland 1995, 1996; Allen et al. 2008). However, it must be remembered that the extent of the precursors is much greater than the shock itself, so any He II emission will be more spatially extended and more featureless than the shocked shell.

Surprisingly, the slow shocks are also quite effective in producing He II emission (see Table 2, column 4). Fully radiative shocks produce He II 4686/Hβ flux ratios in the range of 0.048–0.094 with a peak at about $V_s \sim 120\,\mathrm{km\,s^{-1}}$. This is consistent with the limit to the He II 4686/Hβ flux ratio that can be placed upon the spectrum shown in Fig. 2, taking into account the S/N of this spectrum.

Much higher values can be found in partially radiative shocks, with values of He II 4686/Hβ >0.1 being readily attainable. Since partially radiative shocks will generally be moving into regions of lower density, and observational test would be to see if the fainter regions of the shell are characterized by higher He II 4686/Hβ flux ratios. Unfortunately, the S/N in the blue region of the spectrum is lower than in the red, and a combined spectrum of the faint regions (66–86) is just insufficient to provide a definitive test, since it only constrains He II 4686/H$\beta \lesssim 0.15$.

3.4 Derived shock parameters

In most regions of S26, the measured [S II] ratio $\lambda\lambda$6731/6717 is clearly above the low-density limit of 0.665,[3] even when the measurement errors are taken into account. From Fig. 5 we have already estimated the shock velocity, V_s, and the radiative age parameter, $\log(nt)$. Thus using the observed [S II] $\lambda\lambda$6731/6717 ratio to infer the [S II] density, and the appropriate [S II] compression factor from Table (2), we can infer the pre-shock hydrogen density in each region of the nebula.

The derived shock parameters are listed in Table 3. This gives the following.

(i) Column (1): the region number identified in Fig. 3.
(ii) Column (2): the inferred shock velocity from Fig. 5.
(iii) Column (3): the measured FWHM of the Hα line.
(iv) Column (4): the age parameter $\log(nt)$ inferred from Fig. 5.
(v) Column (5): the log of the inferred electron density, n_e, from the [S II] $\lambda\lambda$6731/6717 ratio, where values of 1.00 indicate that the ratio is measured at its low-density limit.
(vi) Column (6): the inferred pre-shock hydrogen density, n_0.
(vii) Column (7): the age of the shock derived from columns (4) and (6).
(viii) Column (8): the ram pressure of the shock, P/k, derived from columns (2) and (6).

In Fig. 7 we show the correlation between the inferred age of the shock and the density and ram pressure in the shocks. Note that the analysis is insensitive to shock ages $>10^{13}$ s. Broadly speaking, there is an inverse correlation between the pre-shock density and the shock age, and that the pressure in the jet and counterjet regions is larger than the average in the bubble. The inverse correlation between pre-shock density and shock age is to be expected, since the low-density regions can only become radiative over relatively long time-scales.

4 GLOBAL PARAMETERS OF S26

The theory of relativistic jet-driven bubbles was developed in the context of the double lobe radio sources in active galactic nuclei (AGN) over many years by Scheuer (1974), Blandford & Rees (1974), Rawlings & Saunders (1991), Kaiser & Alexander (1999), Begelman (1996) and Bicknell, Dopita & O'Dea (1997). Zealey et al. (1980) developed the theory to apply to the case of the microquasar SS433. In summary, the relativistic jet is shocked when it starts to burrow into the ISM and the overpressure of the backflow carves out a cavity or cocoon around the jet. The back-flowing gas then inflates a larger bubble between the two jets, which behaves like a mass-loss bubble. The detailed physics is given in Dopita & Sutherland (2003). Define the r-axis to be in the direction along the jets, and the z-axis to be the perpendicular direction. If the mean pressure in the cocoon is P, then towards the head of the cocoon (in the r-direction) the mean pressure is higher, because this is defined by the small area, A, over which the termination shock is jittering. Here we can take the pressure as a factor ζ times the average lobe pressure, where typically $\zeta \sim 2$–10. The velocity of advance of the jet and the velocity of the wall shocks surrounding the cavity excavated by the jet are then given by

$$\frac{\mathrm{d}r}{\mathrm{d}t} = \left[\frac{\beta \dot{E}_j}{\rho c A}\right]^{1/2} \sim \zeta^{1/2}\left[\frac{P}{\rho}\right]^{1/2} \quad (1)$$

and

$$\frac{\mathrm{d}z}{\mathrm{d}t} = \left[\frac{P}{\rho}\right]^{1/2}, \quad (2)$$

respectively, where ρ is the density of the pre-shock ISM surrounding the jet head, and $\dot{E}_j$ is the mechanical energy delivered to a single jet moving at a velocity βc, and having an area A.

[3] This value follows from the quantum mechanical sum rule for collision strengths between a singlet and a multiplet state (see equation 3.6 of Dopita & Sutherland 2003), since at low densities the line flux ratio is simply decided by the ratio of the collision strengths from the ground state, corrected by the ratio of energies associated with the individual lines.

Table 3. The inferred shock parameters for each region of S26 defined by Fig. 3.

(1) Spectrum number	(2) V_s (km s^{-1})	(3) FWHM (km s^{-1})	(4) log (nt) (cm^{-3} s)	(5) log n_e (cm^{-3})	(6) log n_0 (cm^{-3})	(7) log t (yr)	(8) log (P/k) (cm^{-3} K)
15	80	122	>13.0	2.20	1.20	4.30	7.22
19	80	97	>13.0	2.30	1.30	4.20	7.32
20	130	150	>13.0	2.76	1.48	4.02	7.92
21	80	129	12.6	2.95	1.95	3.15	7.97
23	80	94	12.0	2.00	0.92	3.58	6.94
24	140	147	>13.0	2.40	1.04	4.46	7.54
25	140	158	>13.0	2.60	1.04	4.46	7.54
26	80	97	12.0	2.40	1.40	3.10	7.42
27	110	106	>13.0	2.40	1.26	4.24	7.55
28	170	153	12.6	2.40	0.92	4.18	7.59
29	170	152	12.6	2.40	0.92	4.18	7.59
30	120	119	>13.0	2.70	1.50	4.00	7.87
31	100	111	12.0	2.00	0.83	3.67	7.04
32	170	166	12.6	2.40	0.94	4.16	7.61
33	170	149	12.6	2.40	0.94	4.16	7.61
34	140	111	12.6	2.05	0.69	4.41	7.19
35	130	131	12.6	2.00	0.74	4.36	7.18
36	170	165	11.7	1.80	0.20	4.00	6.87
37	180	123	11.8	2.20	0.56	3.74	7.28
38	130	97	11.5	1.00	−0.52	4.52	5.92
42	120	123	11.5	1.60	0.18	3.82	6.55
43	190	173	11.8	2.20	0.50	3.80	7.27
44	200	151	11.8	1.80	0.01	4.29	6.82
45	140	98	11.4	2.20	0.58	3.32	7.08
46	120	141	11.3	2.23	0.74	3.06	7.11
47	170	184	11.6	2.00	0.33	3.77	7.00
48	200	185	12.0	2.00	0.34	4.16	7.15
49	170	151	11.6	2.00	0.33	3.77	7.00
50	170	98	11.4	2.35	0.63	3.27	7.30
51	140	192	11.5	1.80	0.24	3.71	6.74
52	140	185	11.4	2.30	0.71	3.19	7.21
53	170	157	11.6	1.80	0.13	3.97	6.80
54	200	125	12.0	2.00	0.34	4.16	7.15
55	200	123	12.0	2.00	0.34	4.16	7.15
56	110	96	11.4	2.35	0.87	3.03	7.16
60	110	193	11.6	2.00	0.52	3.58	6.81
61	140	175	11.3	2.35	0.73	3.07	7.23
62	170	120	11.4	2.00	0.26	3.64	6.93
63	100	160	11.3	1.10	−0.27	4.07	5.94
64	140	155	11.3	2.10	0.48	3.27	6.98
65	120	120	11.1	1.00	−0.57	4.17	5.80
66	140	157	11.2	1.95	0.30	3.35	6.80
67	80	124	11.3	2.30	1.09	2.71	7.11
69	80	107	11.3	2.60	1.39	2.36	7.41
70	140	153	11.2	2.45	0.80	2.90	7.30
71	120	125	11.1	2.15	0.61	2.99	6.98
72	140	128	11.1	2.40	0.75	2.85	7.25
73	110	116	11.1	2.45	0.90	2.70	7.19
74	100	79	10.9	1.00	−0.46	3.86	5.75
75	110	110	11.0	2.30	0.78	2.72	7.07
76	130	145	11.3	1.00	−0.54	4.29	5.90
77	100	108	11.1	2.30	0.87	2.73	7.08
78	100	64	10.9	2.70	1.23	2.17	7.44
79	120	151	11.2	2.40	0.92	2.78	7.29
80	100	123	11.1	1.20	−0.24	3.84	5.97
82	80	68	11.2	1.00	−0.10	3.80	5.92
83	80	79	11.1	2.30	1.20	2.40	7.22
84	120	150	11.2	2.25	0.75	2.95	7.12
86	80	84	11.1	1.00	−0.10	3.70	5.92

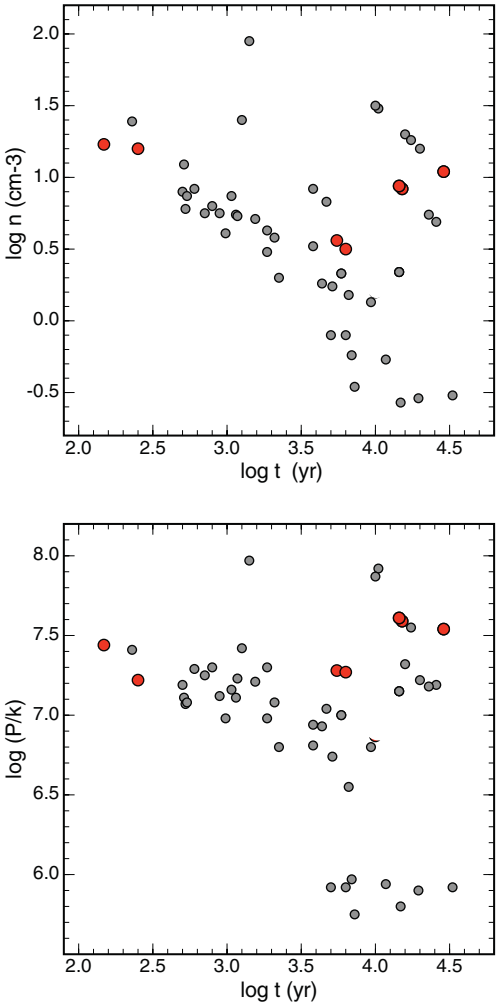

Figure 7. The correlation between inferred age of the shock and either density (upper panel) or the ram pressure (lower panel). The red points on the right represent points in the SE jet and the two red points to the left of these diagrams represent shocks in the NW counterjet. Note the high pressures in both jets and the comparative (radiative) youth of the counterjet shocks.

For the larger bubble between the jets, Zealey et al. (1980) showed that the mass-loss bubble formula for the bubble radius along the minor axis, z, given by Castor, Weaver & McCray (1975) or Weaver et al. (1977) applies

$$z = \alpha^{1/5} \left(\frac{\dot{E}_j}{\rho_z} \right)^{1/5} t^{3/5}, \quad (3)$$

where $\dot{E}_j$ is now understood to be the combined energy flux of both jets, ρ_z is the density along the minor axis and α is a constant. For a bubble containing thermal plasma with a filling factor ϕ, $\alpha = (125/154\pi\phi)$ so that $\alpha^{1/5} = 0.76\phi^{-1/5}$, while for a bubble entirely filled by relativistic plasma with $\gamma = 4/3$, $\alpha = (125/224\pi\phi)$ so that $\alpha^{1/5} = 0.708\phi^{-1/5}$. The latter case (with $\phi \sim 1.0$) is more likely to be valid in the case of S26, since the extent of the non-thermal radio emission is quite similar to that of the optical shell.[4] The age

[4] We are grateful to the referee for reminding us of the subtle distinction between the thermally and the relativistically filled cases.

of the bubble, τ, can then be directly inferred from the radius of the bubble, z, and the expansion velocity in the z-direction; $\tau = (3/5)(z/v_z)$.

The density, pressure and shock velocity in the cocoon around the SE jet can be obtained by averaging the values estimated for spectrum numbers 24, 25, 28, 29, 32, 33 and 34. This gives $v_s(z) = 165\,\mathrm{km\,s^{-1}}$, $P = 6.0 \times 10^{-9}\,\mathrm{dyne\,cm^{-2}}$ and $\rho = 2.2 \times 10^{-23}\,\mathrm{g\,cm^{-3}}$. The likely value of ζ can be estimated by comparing the rate of advance of the jets given by equation (2) with the observations. With $\zeta \sim 4$ the rate of advance of the SE jet of 330 km s^{-1} is reproduced. Applying a similar analysis to the NW counterjet (spectrum numbers 79 and 86) gives $v_s(z) = 130\,\mathrm{km\,s^{-1}}$, $P = 2.5 \times 10^{-9}\,\mathrm{dyne\,cm^{-2}}$, $\rho = 1.5 \times 10^{-23}\,\mathrm{g\,cm^{-3}}$ and a current rate of advance of the NW jet $v_s(r)$, of 260 km s^{-1}, which is also in good agreement to the observations. We may conclude $\zeta \sim 4$. Finally, given that we would expect the pressure at the termination shocks of the jets to fall off as the inverse square of the distance, the ratio of the measured pressures in the two jets should be in proportion to the inverse square of the distance. For S26 this implies a pressure ratio of ∼2.2 which compares well to the observed ratio, 2.4.

The velocity of expansion of the overall mass-loss bubble can be also estimated using the mean of spectra 66, 67, 70 and 72. We find $v_s(z) = 132\,\mathrm{km\,s^{-1}}$, $P = 2.0 \times 10^{-9}\mathrm{dyne\,cm^{-2}}$ and $\rho_z = 1.15 \times 10^{-23}\,\mathrm{g\,cm^{-3}}$. The ratio of $v_s(r)/v_s(z) = 2.5$ compares well with the ratio of the physical size in the r and z directions, $R/Z = 175\,\mathrm{pc}/92\,\mathrm{pc} = 1.9$, showing that the expansion velocity estimates are reasonably consistent with each other.

The age of S26 can now be estimated as $\tau = (3/5)(z/v_z) = 1.3 \pm 0.15 \times 10^{13}$ s or $4.1 \pm 0.5 \times 10^5$ yr. This is somewhat older than the $\sim 2 \times 10^5$ yr estimated by Pakull et al. (2010) thanks to the lower shock velocity estimated here.

The jet energy flux can now be obtained from equation (3). We find $\dot{E}_j = 5.6^{+2.0}_{-1.5} \times 10^{40}\,\mathrm{erg\,s^{-1}}$, identical to the value estimated by Pakull et al. (2010) from the Hβ luminosity. However, they used the theory of fast shocks from Allen et al. (2008), whereas slow shock theory is more appropriate for the vast majority of the shocks in S26. For these, the conversion factor between Hβ (or Hα) flux and total luminosity is lower, and is given by Rich et al. (2010). For shock velocities greater than 120 and less than 200 km s^{-1}, the conversion factor is virtually constant at about 80 (Hα to total luminosity). We therefore estimate the corrected total luminosity of the radiative shocks in S26 to be $L_{\rm rad} = 2.6 \times 10^{40}\,\mathrm{erg\,s^{-1}}$. Using the theory appropriate for a fully filled relativistic bubble in the fully radiative phase, $\dot{E}_j = (112/25)L_{\rm rad} = 1.0 \times 10^{41}\,\mathrm{erg\,s^{-1}}$ ($7.0 \times 10^{40}\,\mathrm{erg\,s^{-1}}$ if filled with thermal plasma). Combining these two approaches, we conclude that the jet energy flux lies in the range of $(4-10) \times 10^{40}\,\mathrm{erg\,s^{-1}}$, in excellent agreement with that estimated by Pakull et al. (2010).

The jet energy flux corresponds to an Eddington luminosity for a 200–700 $\mathrm{M}_\odot$ black hole. However, it is comparable with the X-ray luminosities of the most hyperluminous stellar sources (Swartz et al. 2011), strongly suggesting that S26 belongs to the same population of stellar black holes as the ULX sources. The difference is presumably that S26 is currently attempting to swallow a stellar companion through Roche lobe accretion so that the X-ray luminosity has been transformed to jet energy flux.

By substituting the derived jet energy flux into equation (1) we can estimate the area A of the shocks. We do not have a good estimate of the relativistic β, so retain this factor explicitly to estimate $A \sim 0.38\beta^{-1}\,\mathrm{pc^2}$. If we assume β to be similar to SS433 ($\beta \sim 1/3$), then the jet covers about 1.1 pc^2, implying a collimation angle of about 0.25°.

If the X-ray hotspots are indeed marginally resolved, as claimed by Pakull et al. (2010), then they cover ∼20 pc and subtend an angle of 6° at the central source. Therefore, either the precession angle or 'jittering' of the jets is within a cone opening angle of 6°, or else the jet is decollimated by the same amount. This latter condition would require a very low jet speed, $\beta \sim 0.02$, of a jet velocity of ∼7000 km s^{-1}. Whilst not excluded this seems unlikely, as it would require that a great deal of matter has been processed by the jet. This mass is given by $M = \tau\,\dot{E}_j/(\beta c)^2$. For $\beta = 1/3$ we obtain $M \sim 4\,\mathrm{M}_\odot$, while for $\beta = 0.02$, the mass needed to be processed rises to over 1000 $\mathrm{M}_\odot$. Clearly the jet energy flux cannot be maintained over the lifetime of the bubble unless the jets are fully relativistic. This also suggests that here we are dealing with a bubble filled with relativistic rather than thermal gas. The total energy injected to the bubble over the lifetime of the bubble is given by $E_{\rm tot} = \dot{E}_j\,\tau \sim 8 \times 10^{53}$ erg.

5 CONCLUSIONS

We have shown that the radiative properties of the shell of NGC 7793−S26 can be understood in the context of a model in which the shell is still becoming fully radiative in its NW portions, due to a large-scale density gradient in the ISM. Although the age of the oldest shocks cannot be reliably measured, we can set an age limit comparable with the inferred age of the shell, 4.1×10^5 yr, and we can infer a jet advance velocity in the SE jet of 330 km s^{-1}.

We concur with Pakull et al. (2010) that S26 represents the 'missing link' between the ULX sources and their energetic bubbles, and the less luminous Galactic source SS433 and its nebula, W50. Indeed, the lower jet luminosity we infer here, $\dot{E}_j = (4-10) \times 10^{40}\,\mathrm{erg\,s^{-1}}$, is comparable with the X-ray luminosities of the most hyperluminous stellar sources (Swartz et al. 2011). Unlike SS433, the jets in S26 undergo very little precession, over not more than ±3°.

In conclusion, the central source of S26 is almost certainly a black hole of the typical mass which characterizes the ULX population in a close binary with a more normal star. Given that S26 has processed at least 4 $\mathrm{M}_\odot$ through the jets already, the companion is likely to be an intermediate-mass star which is in the process of being consumed by its unfriendly companion.

ACKNOWLEDGMENTS

We thank the anonymous referee for a careful and professional review, for his/her insight into the nature of this object and its ULX relatives. This paper has been much improved through the referee's input. MAD acknowledges the support from the Australian Department of Science and Education (DEST) Systemic Infrastructure Initiative grant and from an Australian Research Council (ARC) Large Equipment Infrastructure Fund (LIEF) grant LE0775546 which together made possible the construction of the WiFeS instrument. MAD would also like to thank the Australian Research Council (ARC) for support under Discovery project DP0984657. This research has made use of the NASA/IPAC Extragalactic Database (NED) which is operated by the Jet Propulsion Laboratory, California Institute of Technology, under contract with the National Aeronautics and Space Administration. This research has also made use of NASA's Astrophysics Data System.

REFERENCES

Allen M. G., Groves B. A., Dopita M. A., Sutherland R. S., Kewley L. J., 2008, ApJS, 178, 20

Begelman M. C., 1996, in Carilli C. L., Harris D. E., eds, Cygnus A: A Study of a Radio Galaxy. Cambridge Univ. Press, Cambridge, p. 209

Bicknell G. V., Dopita M. A., O'Dea C. P., 1997, ApJ, 485, 112

Blair W. P., Long K. S., 1997, ApJS, 108, 161

Blandford R. D., Rees M. J., 1974, MNRAS, 169, 395

Castro J., Weaver R., McCray R., 1975, ApJ, 200, L107

Dopita M. A., Binette L., 1983, in Danziger J., Gorenstein P., eds, Proc. IAU Symp. 101, Supernova Remnants and Their X-ray Emission. Reidel, Dordrecht, p. 221

Dopita M. A., Sutherland R. S., 1995, ApJ, 455, 468

Dopita M. A., Sutherland R. S., 1996, ApJS, 102, 161

Dopita M. A., Sutherland R. S., 2003, Astrophysics of the Diffuse Universe. Springer, Berlin

Dopita M., Hart J., McGregor P., Oates P., Bloxham G., Jones D., 2007, Ap&SS, 310, 255

Dopita M. et al., 2010, Ap&SS, 327, 245

Jacobs B. A., Rizzi L., Tully R. B., Shaya E. J., Makarov D. I., Makarova L., 2009, AJ, 138, 332

Kaiser C. R., Alexander P., 1999, MNRAS, 305, 707

Koribalski B. S. et al., 2004, AJ, 128, 16

Lasker B. M., 1977, ApJ, 212, 390

López-Sánchez A. R., Dopita M. A., Kewley L. J., Zahid H. J., Nicholls D. C., Scharwächter J., 2012, MNRAS, in press

Mathewson D. S., Ford V. L., Dopita M. A., Tuohy I. R., Long K. S., Helfand D. J., 1983, ApJS, 51, 345

Mathewson D. S., Ford V. L., Dopita M. A., Tuohy I. R., Mills B. Y., Turtle A. J., 1984, ApJS, 55, 189

Mathewson D. S., Ford V. L., Tuohy I. R., Mills B. Y., Turtle A. J., Helfand D. J., 1985, ApJS, 58, 197

McGregor P. J. et al., 2003, Proc. SPIE, 4841, 1581

Pakull M. W., Grisé F., 2008, in AIP Conf. Proc. Vol. 1010, A Population Explosion. Am. Inst. Phys., New York, p. 303

Pakull M. W., Mirioni L., 2002, preprint (astro-ph/0202488)

Pakull M. W., Soria R., Motch C., 2010, Nat, 466, 209

Pannuti T. G., Duric N., Lacey C. K., Ferguson A. M. N., Magnor M. A., Mendelowitz C., 2002, ApJ, 565, 966

Pannuti T. G. et al., 2011, AJ, 142, 20

Pietrzynski G. et al., 2010, AJ, 140, 1457

Rawlings S., Saunders R., 1991, Nat, 349, 138

Raymond J. C., Hester J. J., Cox D., Blair W. P., Fesen R. A., Gull T. R., 1988, ApJ, 324, 869

Read A. M., Pietsch W., 1999, A&A, 341, 8

Rich J. A., Dopita M. A., Kewley L. J., Rupke D. S. N., 2010, ApJ, 721, 505

Scheuer P. A. G., 1974, MNRAS, 166, 513

Schlegel D. J., Finkbeiner D. P., Davis M., 1998, ApJ, 500, 525

Soria R., Pakull M. W., Broderick J. W., Corbel S., Motch C., 2010, MNRAS, 409, 541

Sutherland R. S., Dopita M. A., 1993, ApJ, 88, 253

Swartz D. A., Soria R., Tenant A. F., Yukita M., 2011, ApJ, 741, 49

Weaver R., McCray R., Castor J., Shapiro P., Moore R., 1977, ApJ, 218, 377

Zealey W. J., Dopita M. A., Malin D. F., 1980, MNRAS, 192, 731

This paper has been typeset from a TEX/LATEX file prepared by the author.